Journal of Power Sources 195 (2010) 2014–2022

Contents lists available at ScienceDirect

Journal of Power Sources

journal homepage: www.elsevier.com/locate/jpowsour

# Hierarchical porous cobalt oxide array films prepared by electrodeposition through polystyrene sphere template and their applications for lithium ion batteries

X.H. Xia, J.P. Tu*, J.Y. Xiang, X.H. Huang, X.L. Wang, X.B. Zhao

*State Key Laboratory of Silicon Materials and Department of Materials Science and Engineering, Zhejiang University, Zheda Road, No. 38, Hangzhou, Zhejiang 310027, China*

ARTICLE INFO

*Article history:*
Received 11 August 2009
Received in revised form 1 October 2009
Accepted 2 November 2009
Available online 10 November 2009

*Keywords:*
Cobalt oxide
Polystyrene sphere template
Porous film
Lithium ion batteries

ABSTRACT

Hierarchical porous cobalt oxide ($Co_3O_4$) array films are successfully prepared by electrodeposition through polystyrene sphere monolayer template. The as-prepared $Co_3O_4$ array films exhibit three typical porous structures from non-close-packed bowl array to close-packed bowl array and hierarchical two layer array structures. These $Co_3O_4$ array films have a hierarchical porous structure, in which the skeleton is composed of ordered arrays possessing nanoporous walls. A possible growth mechanism of porous $Co_3O_4$ array films is proposed. As anodes for Li ion batteries, the as-prepared $Co_3O_4$ array films exhibit quite good cycle life and high capacity. The first discharge capacity for the three $Co_3O_4$ array films is 1511, 1475, 1463 mAh $g^{-1}$, respectively, and their initial coulombic efficiencies are as high as 72%. The specific capacity after 50 cycles for the three electrodes is 712, 665 and 640 mAh $g^{-1}$ at 1*C* rate, corresponding to 80%, 75%, 72% of the theoretical value (890 mAh $g^{-1}$), respectively.



## 1. Introduction

In the past decade, extensive research has been launched into the development of alternative anode materials for Li ion batteries [1–5]. Among the explored systems, transition metal oxides such as NiO, CoO, and $Co_3O_4$ have attracted great attention due to their noticeable capacity retention, high electrochemical capacity about three times larger than those of graphite and pretty good high rate performance [6–8]. Compared to other transition metal oxides, spinel cobalt oxide ($Co_3O_4$) is considered as a promising alternative anode material for Li ion batteries because it has shown the highest reversible capacity (890 mAh $g^{-1}$) and the best cycle performance [6,9–12]. Porous nanostructured $Co_3O_4$, with a high surface area and enhanced electrochemical reactivity, is particularly attractive. For example, $Co_3O_4$ nanoparticles, nanotubes and nanowires have been synthesized and enhanced electrochemical performance for Li ion batteries have been found in these systems [13–16].

Despite numerous porous nanostructured $Co_3O_4$ materials have been synthesized and applied for Li ion batteries, these researches focused on nanostructured $Co_3O_4$ power materials [13–19]. In the case of powder materials for Li ion batteries, the active materials need to be mixed with carbon and polymer binders and compressed into pellets. This process risks negating the benefits associated with the reduced particle size and introduces supplementary, undesirable interfaces. For these reasons, the direct growth of porous nanostructured $Co_3O_4$ on various substrates, especially on conducting substrates, is an important issue for their applications [20].

In recent years, two-dimensionally (2D) ordered porous array films induced by colloidal monolayer lithography have elicited much interest due to their distinctive structural features and intriguing properties [21–23]. The typical monolayer colloidal crystal template (MCCT) is an ordered monolayer colloidal microsphere array with a hexagonal close-packed alignment on a certain substrate (typically polystyrene or silica spheres as the template) [24,25]. In general, the interstitial spaces between colloidal spheres are infiltrated with another material and subsequent removal of the template by either wet etching or thermal decomposition leads to the formation of ordered porous structure [26,27]. Among the existing synthetic approaches of target materials infiltration into the colloidal template, electrochemical techniques show unique principles and flexibility in the control of the structure and morphology of porous arrays [28]. Electrochemical deposition is believed to be an ideal method for the fabrication of ordered porous arrays with various morphologies, because it occurs from the electrode surface out through the overlying template, different morphologies of the materials can be obtained via the precise choice of deposition bath and deposition conditions.

By far, there are few reports devoted to the synthesis of ordered porous $Co_3O_4$ array films prepared through the MCCT method and their application for Li ion batteries. Moreover, it is reported that the ordered arrays with a hierarchical pore system would

* Corresponding author. Tel.: +86 571 87952573; fax: +86 571 87952856.
*E-mail address:* tujp@zju.edu.cn (J.P. Tu).

0378-7753/$ – see front matter © 2009 Elsevier B.V. All rights reserved.
doi:10.1016/j.jpowsour.2009.11.009

bestow the possibility to combine the different functionality provided by each type of porosity [29]. For instance, a structure of interconnected macropores whose walls possess finer pores would present increased mass transport through the former and high specific surface area due to the latter. Therefore, it is interesting to design a porous $Co_3O_4$ array with a hierarchical porous system, in which the skeleton is composed of ordered macrobowls possessing nanoporous walls. It is believed that this ordered porous $Co_3O_4$ array will combine the merits of patterned array and nanostructure. Herein, we report a controllable synthesis of porous $Co_3O_4$ arrays with three different morphologies by the combination of electrodeposition and MCCT method. The morphology evolution of porous $Co_3O_4$ arrays is realized via adjusting deposition current: 0.5, 1.0 and 1.5 mA cm$^{-2}$ for 300 s, respectively. More interestingly, these $Co_3O_4$ array films have a hierarchical porous structure, in which the skeleton is composed of ordered arrays possessing nanoporous walls. Furthermore, the as-synthesized porous $Co_3O_4$ arrays have been applied as anode materials for Li ion batteries, which exhibit superior performance and thus promising application.

## 2. Experimental

All solvents and chemicals were of reagent quality and were used without further purification. The monodispersed PS spheres with particle sizes of 1 μm in diameter were purchased from Alfa Aesar Corporation. They were well dispersed in deionized water and prepared as a suspension with concentration of 2.5 wt.% before fabricating colloidal monolayers.

We have successfully electrodeposited porous $Co_3O_4$ array films on indium tin oxide (ITO) and nickel foil substrates through the MCCT method. There was no apparent difference in the coating morphology for different substrates. Thus, the method presented here was very robust and might lead to broad applications. As an illustrative case for morphology, we chose ITO as a substrate. Additionally, the samples for electrochemical measurements of Li ion batteries were prepared on nickel foil substrates.

### 2.1. Assembly of monolayer PS sphere template

The first step was to prepare an ordered monolayer PS spheres by self-assembly. Firstly, a small amount of PS suspension was dropped onto the surface of the clean indium tin oxide (ITO) substrate with a size of 1.5 cm × 1.5 cm. After holding the substrate stationary for 1 min to obtain good dispersion of the suspension, the substrate was then slowly immersed into deionized water. Once the suspension contacted the water's surface, a monolayer of PS spheres was observed on the surface of the water and on the surface of the ITO substrate. To prevent any further additions to the substrate, it was kept immersed. Then, a few drops of 2% dodecyl sodium sulfate solution were added to the water to change the surface tension. As a result, the PS spheres that remained suspended on the surface of the water were pushed aside due to the change in the surface tension. Then the substrate was lifted up through the clear area, making sure that no additional PS spheres were deposited on the monolayer during this process and followed by heating at 110 °C in an oven for 5 min to bond the monolayer with the ITO substrate.

### 2.2. Preparation and characterization of porous $Co_3O_4$ array films

The electrodeposition was performed in a standard three-electrode glass cell at 20 °C, the above template electrode as working electrode, saturated calomel electrode (SCE) as reference electrode and a Pt foil as counter-electrode. The precursor films were electrodeposited from aqueous solution containing 0.9 M $Co(NO_3)_2$ and 0.075 M $NaNO_3$ using a Chenhua CHI660C model Electrochemical Workstation (Shanghai). The electrodeposition experiments were carried out at a constant cathodic current of 0.5, 1.0 and 1.5 mA cm$^{-2}$ for 300 s, respectively. The coulombic efficiency for the electrodeposition of $Co(OH)_2$ is about 98% at 0.5 mA cm$^{-2}$, 95% at 1 mA cm$^{-2}$ and 90% at 1.5 mA cm$^{-2}$, respectively. Afterwards, the samples were immersed in toluene for 24 h to remove the PS sphere template. Finally, the as-prepared sampled were dried at 85 °C, and then annealed at 350 °C for 1.5 h in flowing argon.

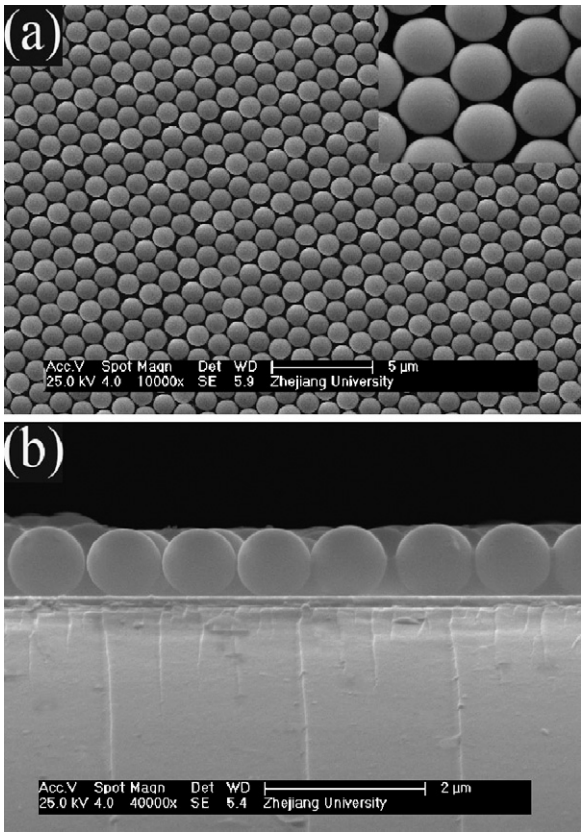


**Fig. 1.** SEM micrographs of (a and b) top and side views of the self-assembled PS sphere template.

The powder from the as-deposited precursor film was analyzed by thermogravimetry (TG) and differential thermal analysis (DTA) under $N_2$ atmosphere at a heating rate of 10 °C min$^{-1}$ in a temperature range of 25–520 °C. The obtained samples were characterized by X-ray diffraction (XRD) using a Rigaku D/max-GA X-ray diffractometer with graphite monochromatized Cu Kα radiation ($k$ = 1.54178 Å). The images and structures of the sample were obtained by field emission scanning electron microscopy (FESEM, FEI SIRION), transmission electron microscopy (TEM, JEM 200 CX 160 kV), high-resolution transmission electron microscope (HRTEM, JEOL JEM-2010F) and Fourier transform infrared (FTIR) measurements (PerkinElmer System 2000 FTIR interferometer). The specific surface areas of the samples were determined by BET (Brunauer–Emmett–Teller) measurements using a NOVA-1000e surface area analyzer.

### 2.3. Electrochemical measurements

Test cells were assembled in an argon-filled glove box using the nickel-supported $Co_3O_4$ array films as working electrode, Li foil as counter-electrode, polypropylene film as separator, and an electrolyte of 1 M LiPF6 in a 50:50 (w/w) mixture of ethylene carbonate and diethyl carbonate. The loading weight for $Co_3O_4$

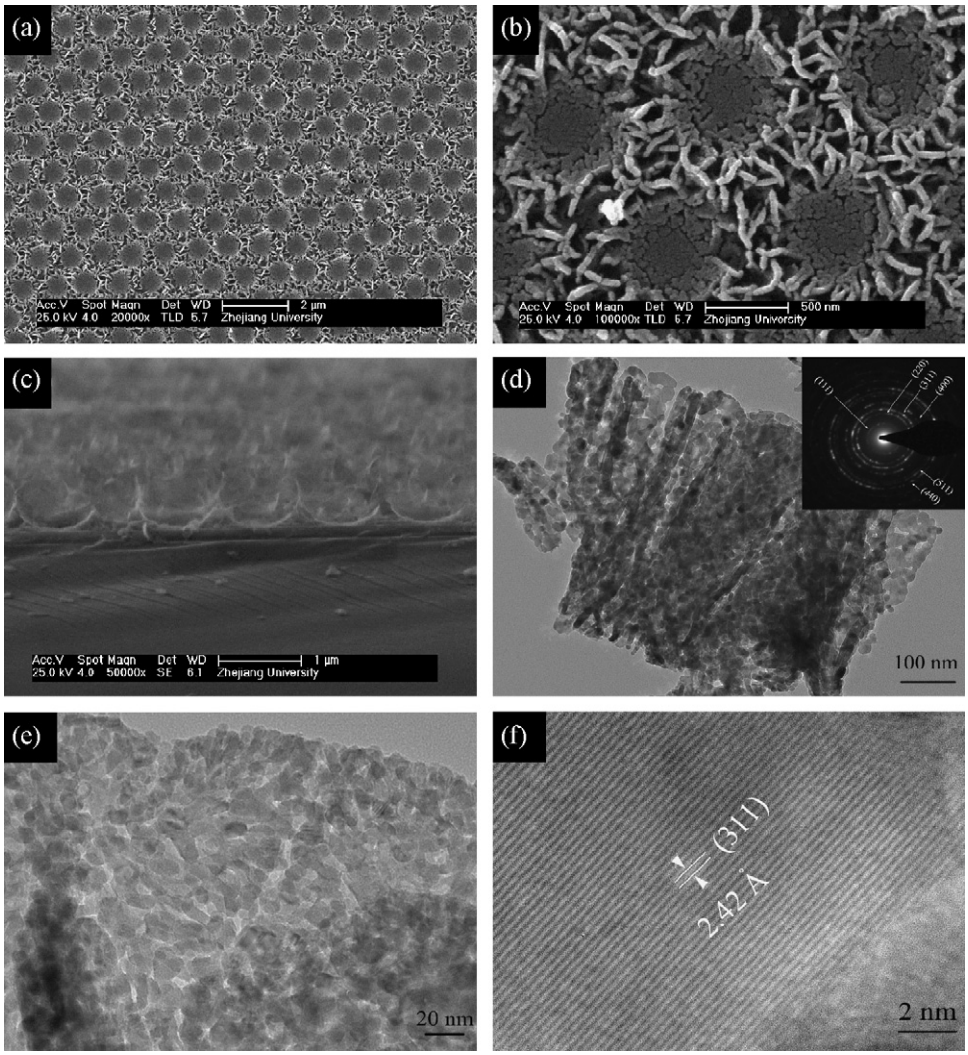


**Fig. 2.** Morphological and structural characterizations of $Co_3O_4$ film electrodeposited at 0.5 mA cm$^{-2}$: (a–c) SEM images; (d and e) TEM images (SAED pattern presented in inset); (f) HRTEM image.

array film electrodeposited at 0.5, 1 and 1.5 mA cm$^{-2}$ is 0.75, 1.4 and 2.0 mg cm$^{-2}$, respectively. Electrochemical measurements were carried out using two-electrode cells with lithium metal as the counter and reference electrodes at 20 °C. The cells were galvanostatically discharged and charged at the current density of 1C (890 mA g$^{-1}$) over a voltage of 0.02–3.0 V versus $Li^+$/Li. Cyclic voltammetry (CV) tests were carried out using the CHI660C at a scanning rate of 0.1 mV s$^{-1}$ between 0 and 3 V.

## 3. Results and discussion

### 3.1. Synthesis and characterization of hierarchical porous $Co_3O_4$ array films

The quality of materials formed through template synthesis depends sensitively on the order and properties of the starting template. Fig. 1a and b shows typical SEM images of the top and side views of the self-assembled PS sphere monolayer. In this case, the PS spheres are organized into a close-packed arrangement with long-range order both parallel and perpendicular to the ITO substrate.

In our experiment, three porous $Co_3O_4$ array films with different morphologies are obtained through PS sphere monolayer template via adjusting deposition current densities: 0.5, 1.0 and 1.5 mA cm$^{-2}$ for 300 s, respectively. Fig. 2 shows the typical SEM images of $Co_3O_4$ array deposited at the current density of 0.5 mA cm$^{-2}$. Notice that the as-synthesized $Co_3O_4$ array exhibits a hierarchical porous structure made up of non-close-packed macrobowels with a diameter of about 500 nm and randomly porous $Co_3O_4$ nanoflakes with a thickness of 35–45 nm (Fig. 2a and b). The bowels in the array are connected by the $Co_3O_4$ nanoflakes, which arrange vertically to the substrate, forming a net-like structure and leaving pores of 40–300 nm. Moreover, note the fact that the sub-micronmeter bowels also exhibit a hierarchical structure composed of $Co_3O_4$ nanoflakes perpendicular to the substrate (Fig. 2b).

Further insight into the microstructure of the nanoflake is obtained by TEM and HRTEM. The flake presents a rough appearance with a continuous porous net-like structure possessing finer pores ranging from 2 to 4 nm (Fig. 2d and e), which are composed of nanoparticles with the size of about 5–12 nm. BET measurement shows that the film has a surface area of 375 m$^2$ g$^{-1}$. The pore size distribution shows a peak at 3 nm (Fig. S1a, see supporting information). In addition, all diffraction rings in the selected area electronic diffraction (SAED) pattern of the nanoflake can be indexed with the spinel $Co_3O_4$ phase (JCPDS 42-1467), indicating that the $Co_3O_4$ array is polycrystalline in nature. Furthermore, the measured lattice spacing of 2.42 Å is in good agreement with the (3 1 1) interplanar distance of the $Co_3O_4$ phase (Fig. 2f).

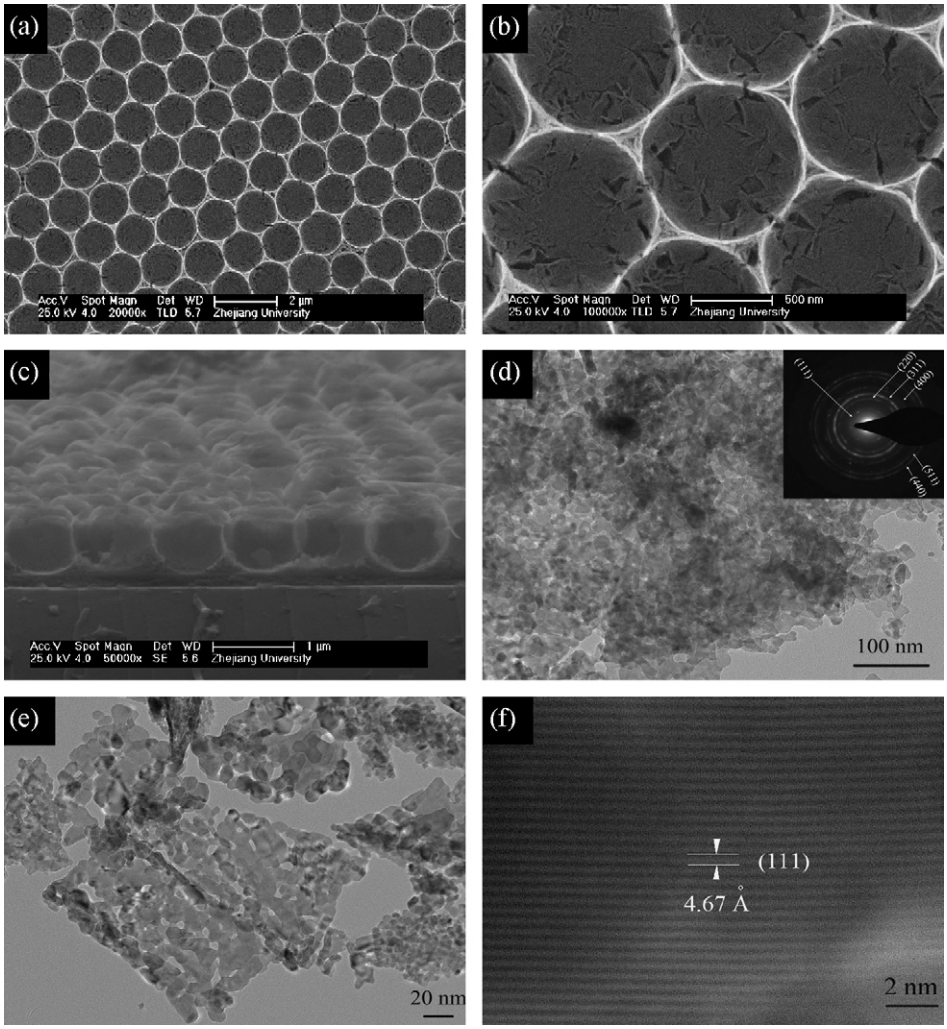


**Fig. 3.** Morphological and structural characterizations of $Co_3O_4$ film electrodeposited at 1.0 mA cm$^{-2}$: (a–c) SEM images; (d and e) TEM images (SAED pattern presented in inset); (f) HRTEM image.

The SEM and TEM images of the $Co_3O_4$ array film deposited at 1.0 mA cm$^{-2}$ are shown in Fig. 3. The morphology of the $Co_3O_4$ array film is quite different from that obtained at 0.5 mA cm$^{-2}$. The as-prepared $Co_3O_4$ film is arranged in an ordered hexagonal close-packed bowel-like array (Fig. 3a–c) as what is usually observed in the literature [30,31]. The skeleton of the array film is made up of macrobowels with a diameter of 1 μm. It is important to notice that the bowls contains a lot of pores ranging from 50 to 200 nm made up of nanoflakes and the interstices between bowels are also filled with $Co_3O_4$ nanoflakes (Fig. 3b). Meanwhile, the flake also exhibits a highly porous structure with the diameter of pores ranging from 5 to 15 nm, composed of nanoparticles with the sizes of about 8–20 nm (Fig. 3d and e), bigger than those of film obtained at 0.5 mA cm$^{-2}$. The pore size distribution is supported by the BET result with a peak at 12 nm (Fig. S1b).

Compared to the film deposited at 0.5 mA cm$^{-2}$, the film deposited at 1.0 mA cm$^{-2}$ shows a surface area of 317 m$^2$ g$^{-1}$. Besides, the SAED pattern reveals the existence of spinel polycrystalline $Co_3O_4$ and the lattice fringes with a lattice spacing of about 4.67 Å nm corresponds to the (1 1 1) planes of $Co_3O_4$.

In the case of $Co_3O_4$ array deposited at 1.5 mA cm$^{-2}$, a hierarchical structure of the $Co_3O_4$ array film is illustrated by SEM in Fig. 4a–d. The as-prepared $Co_3O_4$ array film consists of two parts: the upper part is randomly porous net-like $Co_3O_4$ and the lower part is $Co_3O_4$ monolayer hollow-sphere array (Fig. 4e). The special hierarchical structure can be more clearly seen when the film is detached from the substrate by a blade. After detachment of the $Co_3O_4$ array film, the bottom of the film shows an ordered bowel-like array (Fig. 4c) and a cavity array layer of $Co_3O_4$ (Fig. 4d) is left on the ITO substrate. Combining these patterns, it is reasonable that the as-prepared $Co_3O_4$ film has a two-layer structure: lower part is composed of $Co_3O_4$ monolayer hollow-sphere array and the upper part is randomly porous net-like $Co_3O_4$. Similarly, nanoporous structure is observed in the $Co_3O_4$ flake with pore diameter of 10–30 nm (Fig. 4f and g). The nanoparticle size is in the range of 15–30 nm. The SAED pattern and HRTEM analyses of the flake are similar to those of Fig. 2d and e, also displaying crystalline structure (Fig. 4h). The film exhibits a relatively small surface area of 243 m$^2$ g$^{-1}$ as well as two pore size distribution peaks at 10 and 22 nm, respectively (Fig. S1c).

From the SEM and TEM results above, it is clearly seen that all the as-prepared $Co_3O_4$ films exhibit porous structures with a hierarchical pore system. They all have a structure of interconnected macropores whose walls possess finer pores, which would present increased mass transport through the former and high specific surface area due to the latter. The porous structures may lead to the enhancement of electrochemical properties because of their porosity and higher surface area. A larger electrode/electrolyte contact area and a shorter diffusion length of lithium ions can be obtained in these porous structures, leading to lower inner resistance, which

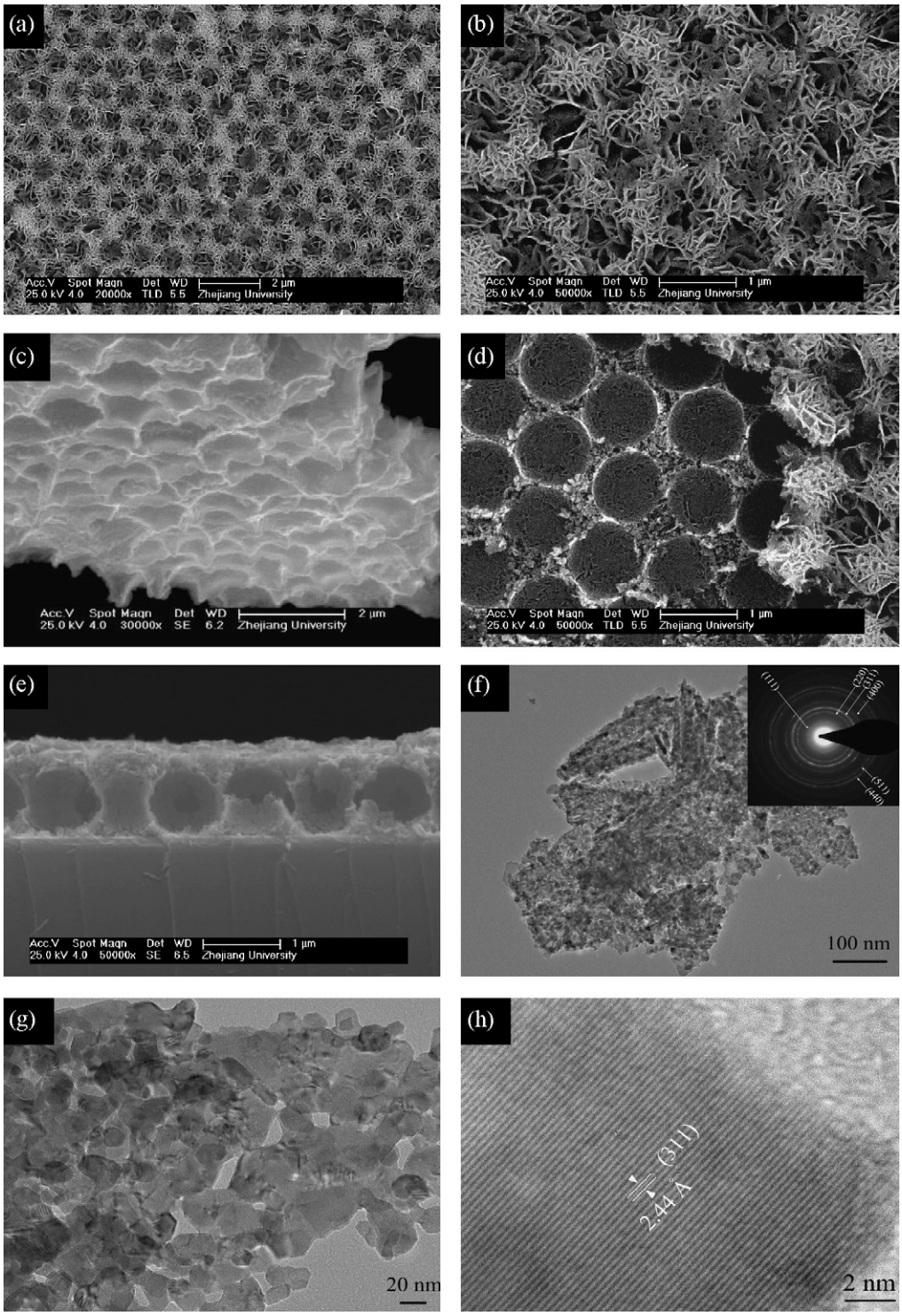


**Fig. 4.** Morphological and structural characterizations of $Co_3O_4$ film electrodeposited at 1.5 mA cm$^{-2}$: (a and b) SEM images of top views (c) typical SEM image of the hierarchically porous-structured film detached from the substrate (d) the residual pattern left on the substrate of the detached film (e) side view of the film; (f and g) TEM images (SAED pattern presented in inset); (h) HRTEM image.

is beneficial to get higher specific capacity and better cycling stability even at high discharge-charge current density [9]. In addition, it is believed that electrochemical reactions between $Co_3O_4$ and Li ion firstly occur at grain boundaries and on grain surfaces. It is inferred that small particle size allows the easy diffusion of ions among them and provides much more active reaction area. Therefore, in our case, better electrochemical performance for the film deposited at 0.5 mA cm$^{-2}$ can be anticipated.

The change of composition and phase is investigated by XRD and FTIR. The diffraction peaks of precursor film are in good agreement with the patterns of layered α-$Co(OH)_2$ (JCPDS 74-1057) (Fig. 5a), similar to those reported by other authors [32,33]. From patterns a–c in Fig. 5, the films show diffraction peaks at 18.9°, 31.2°, 36.9°, 44.8°, 59.2° and 65.2°, which correspond to (1 1 1), (2 2 0), (3 1 1), (4 0 0), (5 1 1) and (4 4 0) crystal planes of spinel $Co_3O_4$ phase (JCPDS 42-1467), respectively, indicating that the polycrystalline $Co_3O_4$

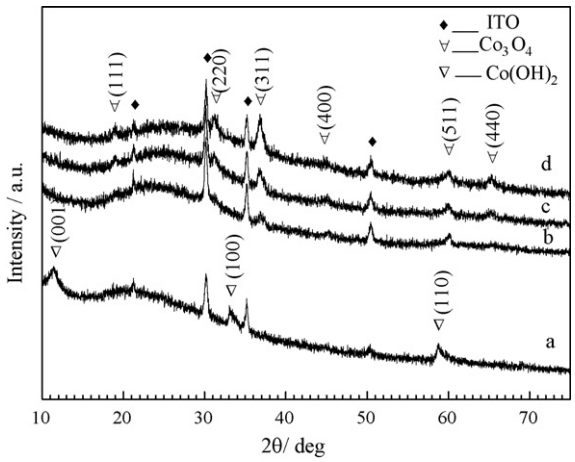


**Fig. 5.** XRD patterns of films deposited on ITO substrate: (a) as-deposited precursor film, (b) $Co_3O_4$ film electrodeposited at 0.5 mA cm$^{-2}$, (c) $Co_3O_4$ film electrodeposited at 1.0 mA cm$^{-2}$ and (d) $Co_3O_4$ film electrodeposited at 1.5 mA cm$^{-2}$.

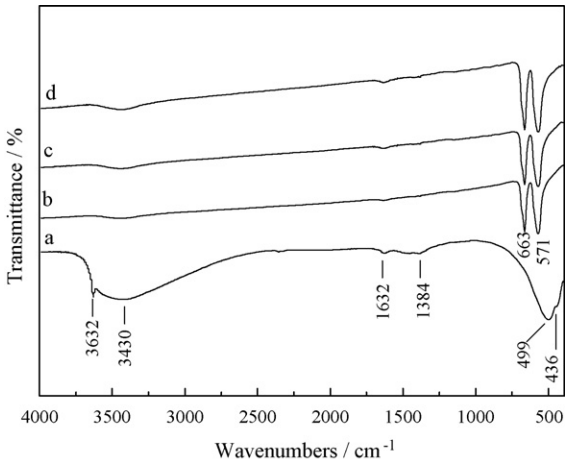


**Fig. 6.** The FTIR spectra of powders from (a) as-deposited precursor film, (b) $Co_3O_4$ film electrodeposited at 0.5 mA cm$^{-2}$, (c) $Co_3O_4$ film electrodeposited at 1.0 mA cm$^{-2}$ and (d) $Co_3O_4$ film electrodeposited at 1.5 mA cm$^{-2}$.

have formed after heat treatment, which are consistent with the TEM results. Meanwhile, the crystallinity of $Co_3O_4$ film increases as the deposition current density increases, which is due to the more deposition amount of $Co_3O_4$ induced by the higher current density. Additionally, the main weight loss of the precursor film is in the temperature range of 150–300 °C, suggesting decomposition of cobalt hydroxide to the formation of $Co_3O_4$. The 12% mass loss is consistent with the expected value for a stoichiometric $Co(OH)_2$ brucite (Fig. S2). The phase change is also confirmed by FTIR results (Fig. 6). In the spectrum of the precursor film, the peak around 3632 cm$^{-1}$ is characteristic of non-hydrogen bonds O–H stretching vibrations of α-$Co(OH)_2$. A broad OH band centered 3420 cm$^{-1}$ is indicative of hydrogen bonded water within the film structure and the band at 1650 cm$^{-1}$ corresponds to the angular deformation of molecular water. The sharp peak around 1384 cm$^{-1}$ comes from stretching vibration of $NO_3^-$, which possibly are intercalated in the layered hydrotalcite-like structure during the formation of α-$Co(OH)_2$. The bands at 500 and 436 cm$^{-1}$ correspond to $\delta$(OH) and $\upsilon$(CoO) vibrations, respectively. After heat treatment, the 3632, 500 and 436 cm$^{-1}$ peaks disappear completely and two very strong peaks centered at 663 and 571 cm$^{-1}$ characteristic of spinel $Co_3O_4$ are observed [20], indicating thorough conversion of α-$Co(OH)_2$ to $Co_3O_4$.

### 3.2. Formation mechanism

The formation of α-$Co(OH)_2$ by electrochemical deposition has been well studied in earlier work. The electrodeposition process of α-$Co(OH)_2$ includes an electrochemical reaction and a precipitation reaction expressed as follows [34,35]:

$$NO_3^- + H_2O + 2e^- \rightarrow NO_2^- + 2OH^- \quad (1)$$

$$Co^{2+} + 2OH^- \rightarrow Co(OH)_2 \quad (2)$$

In this electrochemical reduction process, metallic Co cannot form because the reaction potential of $Co^{2+}$/Co is much more negative than that of $NO_3^-/NO_2^-$(−0.28 V versus 0.01 V) [36]. The as-electrodeposited $Co(OH)_2$ film according to Eqs. (1) and (2) exhibits a porous structure consisting of randomly net-like arranged nanoflakes with (0 0 1) oriented. This preferential growth is because that $Co(OH)_2$ crystal has a layered structure of the $CdI_2$ type, which shows weak interaction between layers and strong binding within the layered planes, that is, the surface energy of the layered (0 0 1) plane is the lowest. Thus, $Co(OH)_2$ will preferentially grow along the layered plane after the formation of its nuclei. Also, due to the directional deposition under the electrical potential, only nuclei oriented with their (0 0 1) plane vertical to the substrate and the PS surface will grow preferentially, leading to the final formation of porous $Co(OH)_2$ films [37], which is confirmed in our experiment. The $Co(OH)_2$ film electrodeposited without PS sphere template exhibits a randomly porous structure composed of nanoflakes perpendicular to the substrate (See Fig. S3). The SAED pattern indicates that the $Co(OH)_2$ flake grows along (0 0 1) orientation (Fig. S3e). The corresponding $Co_3O_4$ film converted from the $Co(OH)_2$ film maintains the porous structure made up of interconnected nanoflakes arranging vertically to the substrate and leaving pores of 20–300 nm (see Fig. S4). Thus, it is concluded that the $Co(OH)_2$ nucleate and grow in the interstitial sites between PS spheres leading to different $Co_3O_4$ array films after heat treatment process.

The proposed mechanism for growing porous $Co_3O_4$ array films is schematically illustrated in Fig. 7. Three typical $Co_3O_4$ array films with different morphologies are obtained by controlling the deposition current density. We find that the thickness of film is a key parameter for growing different $Co_3O_4$ array films. When the thickness of $Co_3O_4$ nanoflake is less than the radius of PS sphere, the $Co_3O_4$ film shows a non-close-packed bowl array structure and the interstitial space are filled with randomly net-like $Co_3O_4$ nanoflakes perpendicular to the substrate (Fig. 7a). With the increase of the thickness up to the radius of PS sphere, the interstitial space below the radius is filled with $Co_3O_4$ nanoflakes leading to a close-packed bowl-like array film (Fig. 7b). Finally, a hierarchical two layer porous $Co_3O_4$ array film is formed as

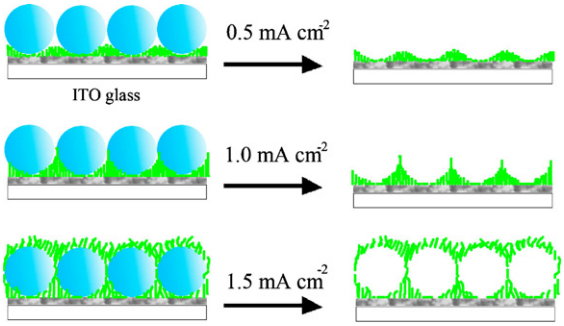


**Fig. 7.** Schematic illustration for the formation of different hierarchical porous-structured $Co_3O_4$ films: (a) at the current of 0.5 mA cm$^{-2}$, (b) at the current of 1.0 mA cm$^{-2}$ and (c) at the current of 1.5 mA cm$^{-2}$.

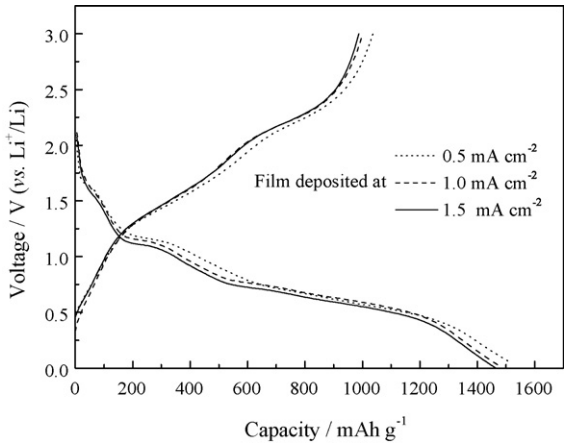


**Fig. 8.** The first discharge–charge curves for the three $Co_3O_4$ film electrodes.

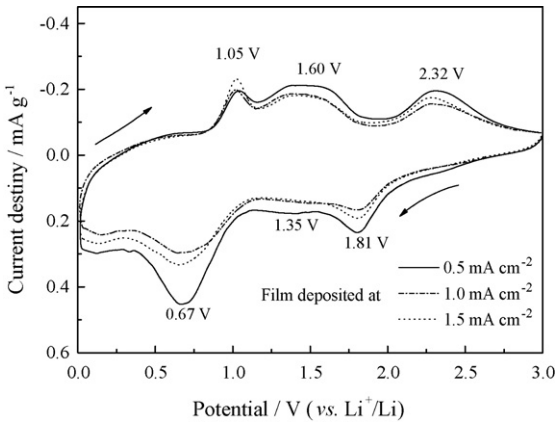


**Fig. 9.** Cyclic voltammograms of three $Co_3O_4$ film electrodes in the potential region of 0–3.0 V at a scanning rate of 0.1 mV $s^{-1}$ at the second cycle.

the film thickness increases more than the diameter of PS sphere (Fig. 7c).

In addition, the effect of the deposition current density on the morphologies of films obtained under the same total charge of the electrolytic deposition is investigated (Fig. S5). The three films exhibit similar morphologies and all show ordered arrays made up of macrobowls with a diameter of about 1 μm. The film deposited at lower current density contains much more random pores in the individual bowl than those obtained at higher current density. We speculate that the flake obtained at higher current density is thicker resulting in compacter bowl-like structure.

### 3.3. Electrochemical analysis

The electrochemical performance of as-prepared porous $Co_3O_4$ array films are evaluated by standard method based on $Co_3O_4$/Li cells, where $Co_3O_4$ electrodeposited on polished nickel foil and lithium foil serve as positive and negative electrode respectively. There is no apparent difference in the coating morphologies of $Co_3O_4$ array films on ITO and polished nickel foil substrates (Fig. S6). Fig. 8 shows the first two discharge–charge curves for the three porous $Co_3O_4$ film electrodes measured between 0.02 V and 3.0 V versus Li/$Li^+$ at 1*C* rate (1*C* = 890 mA $g^{-1}$). Similar discharge–charge behaviors are noticed for the three film electrodes. Taking the $Co_3O_4$ film electrode deposited at 0.5 mA $cm^{-2}$ for example, in the potential range of 1.1–1.7 V, two voltage plateaus at about 1.65 and 1.15 V are noticed, which are generally attributed to reduction process from $Co_3O_4$ to CoO and $Li_xCo_3O_4$, respectively. Then these intermediates further decompose into Co and $Li_2O$ at the third voltage plateau of 0.75 V followed by a sloping curve down to the cutoff voltage of 0.02 V. These three features are in agreement with the previous reports [38,39]. The first discharge capacity for three electrodes is 1511, 1475, 1463 mAh $g^{-1}$, respectively, higher than the theoretical value 890 mAh $g^{-1}$, which is due to the formation of solid electrolyte interphase (SEI) in the first discharge [40,41]. This phenomenon happens in all transition metal oxides, including NiO, FeO, CoO, $Co_3O_4$ and CuO [9–12]. The corresponding initial coulombic efficiency for three electrodes is 72%, 69% and 68%, respectively. These values are comparable to those obtained from $Co_3O_4$ powder materials with nanostructures such as nanotube and nanoparticle (about 70%) [13,14].

To understand the electrochemical process in detail, the CV profiles of the three electrodes are recorded in Fig. 9. The CV curves for the three electrodes are quite the same, but much different and more complex than those obtained from powder electrodes. For the $Co_3O_4$ powder electrodes, the CV curves at the second cycle always exhibit one or two reduction peaks in the cathodic process and one oxidation peak in the anodic process [13–19], however, in our case, three reduction and oxidation peaks are observed. It has been reported that the electrochemical reaction mechanism of Li with $Co_3O_4$ differs from the classical mechanisms of reversible $Li^+$ insertion/deinsertion into host structures or on lithium alloying reactions and involves the formation and decomposition of $Li_2O$ accompanying the reduction and oxidation of metal Co [6,42]. To date, numerous mechanisms of Li with $Co_3O_4$ have been proposed, but the specific mechanism is still unclear. It is well accepted that the reactions between Li with $Co_3O_4$ involves multistep electrochemical processes. According to the work of Larcher et al. [38], there exist two competing mechanisms to research the full decomposition of the $Co_3O_4$ into metallic Co and $Li_2O$. One involves the reduction of $Co_3O_4$ into CoO and $Li_2O$ while the other is the formation of $Li_xCo_3O_4$. Then both intermediates decompose into Co nanograins and $Li_2O$ during further reduction. The corresponding electrochemical reactions can be described as follows [38,42]:

$$Co_3O_4 + 2Li^+ + 2e^- \leftrightarrow Li_2O + 3CoO \quad (3)$$

$$3CoO + 6Li^+ + 6e^- \leftrightarrow 3Li_2O + 3Co \quad (4)$$

or

$$Co_3O_4 + xLi \leftrightarrow LixCo_3O_4 \quad (5)$$

$$LixCo_3O_4 + (8-x)Li \leftrightarrow 4Li_2O + 3Co \quad (6)$$

Our results are in generally agreement with what reported by Larcher et al. [38] and different from the results of Du et al. and Li et al. [13,15]. In the cathodic process, three main reduction peaks are well resolved, including a main reduction peak around 0. 67 V, a low-density peak near 1.35 V and a peak around 1.81 V. Considering the discharge curves in Fig. 8, the three reduction peaks correspond to the reduction of intermediates (CoO or $LixCo_3O_4$) to metallic Co, lithium intercalation into the spinel cobalt oxide to form $LixCo_3O_4$ and conversion from $Co_3O_4$ to CoO, respectively. During the following anodic process, two peaks at 1.05 and 1.60 V are attributed to the formation o $LixCo_3O_4$ and CoO, respectively. The broad peak around 2.32 V corresponds to the oxidation of intermediates leading to the formation of $Co_3O_4$. It is also noticed that the film electrode deposited at 0.5 mA $cm^{-2}$ exhibits the highest current density indicating that the film with non-closed packed bowl array structure has higher electrochemical activity, which is mainly due to its biggest surface area and porosity.

Fig. 10 shows the specific capacity for the three $Co_3O_4$ array films at four different rates. The three films sustain and deliver almost 100% of the theoretical capacity at 0.2*C* rate, 86%, 82% and 79% at 1*C* rate, 81%, 79%, 77% at 2*C* rate, 71%, 68%, 66% at 3*C* rate, respectively. Fig. 11 shows the capacity retention properties of the three

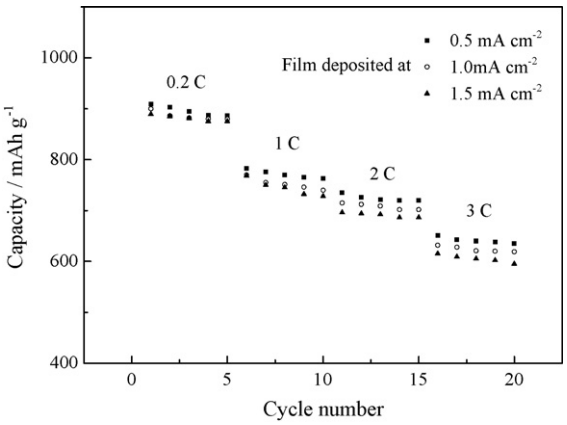


**Fig. 10.** Capacity for the three $Co_3O_4$ film electrodes at four different rates.

electrodes at 1*C* rate. The three $Co_3O_4$ film electrodes are found to sustain and deliver 80%, 75%, and 72% of the theoretical value at 1*C* rate after 50 cycles, respectively. Additionally, the specific capacity after 50 cycles at 2*C* rate for the three electrodes is 671, 625 and 590 mAh $g^{-1}$, corresponding to 75%, 70%, 66% of the theoretical value, respectively (Fig. S7), demonstrating the capability for a high cycling rate. It should be mentioned that nearly 100% capacity retention have been reported before [6,12,13], however, such excellent capacity retention are observed only for first several cycles or the testing was performed at a much lower current rate (≤0.2*C*). In our case, the cycling performance is tested under much higher current rate (≥1*C* rate). Even so, the cycling performance of the three electrodes is still better than those of $Co_3O_4$ micrometer particles [39,43,44], and sputtered $Co_3O_4$ film with compact structure [45]. The highly porous structure is responsible for the improvement of electrochemical performance. Its high porosity and surface area can facilitate the contact between electrolyte and the oxide surface. Furthermore, the nanoflaky network with open spaces between individual nanoflake allows the easier diffusion of Li ion among them. All these contribute to the improvement of electrochemical performance. In addition, the best cycling performance for film with non-closed packed bowl array structure is obtained mainly due to its biggest surface area and huge porosity. In addition, its enhanced electrochemical performance is also related to its relatively low film thickness, which facilitates electrolyte soaking into the particles and shortens the Li ion diffusion paths within the $Co_3O_4$ flake. On the other hand, it should note the fact that the high porosity leads to the low volumetric capacity of the electrode and the low volumetric energy density of the batteries.

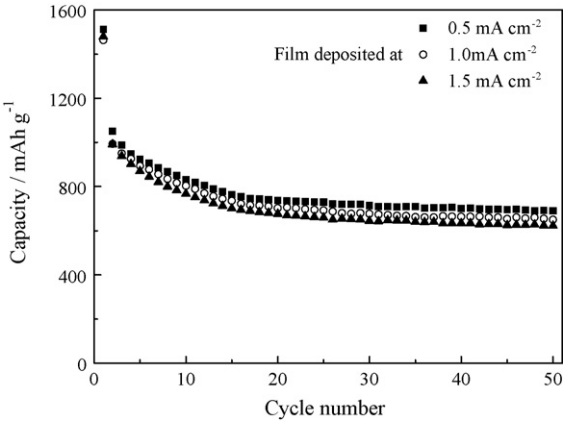


**Fig. 11.** Cycling performance of three $Co_3O_4$ film electrodes at 1*C* rate (1*C* = 890 mA $g^{-1}$).

## 4. Conclusions

In summary, hierarchical porous $Co_3O_4$ array films with three different morphologies from non-close-packed bowl array to close-packed bowl array and hierarchical two-layer array structures have been successfully prepared by electrodeposition through PS sphere monolayer template. The morphology evolution can be realized by controlling the thickness of film via adjusting the deposition current density. The as-prepared $Co_3O_4$ array films exhibit a highly porous structure of interconnected macropores whose walls possess finer pores. These hierarchical porous $Co_3O_4$ array films are prepared by a low-cost and facile method in a controlled process combining the merits of both patterned arrays and nanoflakes, therefore will have promising applications in sensing, Li-ion batteries, field-emission and electrochromic devices. As a preliminary test, such hierarchical porous $Co_3O_4$ array films as anode materials for Li ion batteries have been investigated. They exhibit noticeable cycling performance and discharge capacities, especially for the film with non-close-packed bowl array structure. The enhanced electrochemical performance is attributed to the high porosity and surface area, which facilitate the contact between electrolyte and the oxide surface and provide shorter diffusion length for Li ion leading to higher electrochemical activity.

## Acknowledgement

The authors would like to acknowledge financial support from Zhejiang University K.P. Chao's High Technology Development Foundation (Grant No. 2008ZD001).

## Appendix A. Supplementary data

Supplementary data associated with this article can be found, in the online version, at doi:10.1016/j.jpowsour.2009.11.009.

## References

[1] Y. Idota, T. Kubota, A. Matsufuji, Y. Maekawa, T. Miyasaka, Science 276 (1997) 1395.
[2] M. Winter, J.O. Besenhard, M.E. Spahr, P. Novak, Adv. Mater. 10 (1998) 725.
[3] J.M. Tarascon, M. Armand, Nature 414 (2001) 359.
[4] A.S. Arico, P. Bruce, B. Scrosati, J.M. Tarascon, W.V. Schalkwijk, Nat. Mater. 4 (2005) 366.
[5] F. Cheng, Z. Tao, J. Liang, J. Chen, Chem. Mater. 20 (2008) 667.
[6] P. Poizot, S. Laruelle, S. Grugeon, L. Dupont, J.M. Tarascon, Nature 407 (2000) 496.
[7] X.H. Huang, J.P. Tu, Y.Z. Yang, J.Y. Xiang, Electrochem. Commun. 10 (2008) 16.
[8] X.H. Huang, J.P. Tu, X.H. Xia, X.L. Wang, J.Y. Xiang, L. Zhang, Y. Zhou, J. Power Sources 188 (2009) 588.
[9] X.H. Huang, J.P. Tu, Z.Y. Zeng, J.Y. Xiang, X.B. Zhao, J. Electrochem. Soc. 155 (2008) A438.
[10] D. Larcher, D. Bonnin, R. Cortes, I. Rivals, L. Personaz, J.M. Tarascon, J. Electrochem. Soc. 150 (2003) A1643.
[11] A. Debart, L. Dupont, P. Poizot, J.B. Leriche, J.M. Tarascon, J. Electrochem. Soc. 148 (2001) A1266.
[12] J. Do, C. Weng, J. Power Sources 159 (2006) 323.
[13] N. Du, H. Zhang, B. Chen, J. Wu, X.Y. Ma, Z. Liu, Y. Zhang, D.R. Yang, X.H. Huang, J.P. Tu, Adv. Mater. 19 (2007) 4505.
[14] X.W. Lou, D. Deng, J.Y. Lee, J. Feng, L.A. Archer, Adv. Mater. 20 (2008) 258.
[15] W.Y. Li, L.N. Xu, J. Chen, Adv. Funct. Mater. 15 (2005) 851.
[16] K.T. Nam, D. Kim, P.J. Yoo, C. Chiang, N. Meethong, P.T. Hammond, Y. Chiang, A.M. Belcher, Science 312 (2006) 885.
[17] C. Vidal-Abarca, P. Lavela, J.L. Tirado, Electrochem. Solid-State Lett. 11 (2008) A198.
[18] K.M. Shaju, F. Jiao, A. Debart, P.G. Bruce, Phys. Chem. Chem. Phys. 9 (2007) 1837.
[19] W. Yao, J. Yang, J. Wang, Y. Nuli, J. Electrochem. Soc. 155 (2008) A903.
[20] Y. Li, B. Tan, Y. Wu, J. Am. Chem. Soc. 128 (2006) 14258.
[21] Y. Li, B. Tan, Y. Wu, Nano Lett. 8 (2008) 265.
[22] M.C. Orilall, N.M. Abrams, J. Lee, F.J. DiSalvo, U. Wiesner, J. Am. Chem. Soc. 130 (2008) 8882.

[23] A. Stein, F. Li, N.R. Denny, Chem. Mater. 20 (2008) 649.
[24] Q. Zhou, J. Zhao, W. Xu, H. Zhao, Y. Wu, J. Zheng, J. Phys. Chem. C 112 (2008) 2378.
[25] Q. Zhou, H. Zhao, F. Pang, Q. Jing, Y. Wu, J. Zheng, J. Phys. Chem. C 111 (2007) 514.
[26] P.N. Bartlett, J.J. Baumberg, P.R. Birkin, M.A. Ghanem, M.C. Netti, Chem. Mater. 14 (2002) 2199.
[27] M. Sadakane, T. Horiuchi, N. Kato, C. Takahashi, W. Ueda, Chem. Mater. 19 (2007) 5779.
[28] Y. Tan, S. Srinivasan, K.S. Choi, J. Am. Chem. Soc. 127 (2005) 3596.
[29] L.A. Villaescusa, A. Mihi, I. Rodrguez, A.E. Garca-Bennett, H. Mguez, J. Phys. Chem. B 109 (2005) 19643.
[30] G. Duan, W. Cai, Y. Luo, Z. Li, Y. Lei, J. Phys. Chem. B 110 (2006) 15729.
[31] Y. Li, W. Cai, G. Duan, Chem. Mater. 20 (2008) 615.
[32] V. Gupta, T. Kusahara, H. Toyama, S. Gupta, N. Miura, Electrochem. Commun. 9 (2007) 2315.
[33] Z.P. Xu, H.C. Zeng, Chem. Mater. 11 (1999) 67.
[34] W. Zhou, J. Zhang, T. Xue, D. Zhao, H. Li, J. Mater. Chem. 18 (2008) 905.
[35] S.L. Chou, J.Z. Wang, H.K. Liu, S.X. Dou, J. Electrochem. Soc. 155 (2008) A926.
[36] G.H.A. Therese, P.V. Kamath, Chem. Mater. 12 (2000) 1195.
[37] G. Duan, W. Cai, Y. Luo, F. Sun, Adv. Funct. Mater. 17 (2007) 644.
[38] D. Larcher, G. Sudant, J.B. Leriche, Y. Chabre, J.M. Tarascon, J. Electrochem. Soc. 149 (2002) A234.
[39] R. Yang, Z. Wang, J. Liu, L. Chen, Electrochem. Solid-State Lett. 7 (2004) A496.
[40] Y.M. Kang, K.T. Kim, K.Y. Lee, S.J. Lee, J.H. Jung, J.Y. Lee, J. Electrochem. Soc. 150 (2003) A1538.
[41] Y.M. Kang, M.S. Song, J.H. Kim, H.S. Kim, M.S. Park, J.Y. Lee, H.K. Liu, S.X. Dou, Electrochim. Acta 50 (2005) 3667.
[42] P. Poizot, S. Larunelle, S. Grugeon, J.M. Tarascon, J. Electrochem. Soc. 149 (2002) A1212.
[43] G.X. Wang, Y. Chen, K. Konstantinov, M. Lindsay, H.K. Liu, S.X. Dou, J. Power Sources 109 (2002) 142.
[44] G. Binotto, D. Larcher, A.S. Prakash, R.H. Urbina, M.S. Hegde, J.M. Tarascon, Chem. Mater. 19 (2007) 3032.
[45] C.L. Liao, Y.H. Lee, S.T. Chang, K.Z. Fung, J. Power Sources 158 (2006) 1379.